Acta Astronautica 213 (2023) 385–391

Contents lists available at ScienceDirect

Acta Astronautica

journal homepage: www.elsevier.com/locate/actaastro

Research paper

Deflector shape impact on aero-acoustic noise generation and propagation

M.S. Escartí-Guillem [a,b,*], S. Hoyas [b], L.M. García-Raffi [b]

[a] R&D Department, Comet Ingeniería, Convento Carmelitas, 2, Valencia, 46010, C.V., Spain
[b] Instituto Universitario de Matemática Pura y Aplicada, Universitat Politècnica de València, Camino de Vera s/n, 46022, València, Spain

ARTICLE INFO

Keywords:
Launch noise
Prediction
CFD
Deflector shape

ABSTRACT

The acoustic pressure level generated during lift-off and the associated vibrations can significantly affect the payload of a launch vehicle. Optimizing the plume deflector is one of the most effective methods to reduce this noise. Considering the Vega launcher as a case of study, different deflectors are studied: flat, inclined at 30°, and wedge. The approach followed is to use the unsteady Navier–Stokes equations to solve both the noise generation and the propagation. First, it has been observed that the blast wave, due to the ignition overpressure, is independent of the deflector geometry. However, the predominant acoustic waves are due to the impact of the jet with the deflectors. The analysis has shown that the flat deflector generates more shock waves and propagates the acoustic waves equally in all directions so that more acoustic loads reach the fairing. The inclined deflector causes a plate shock and intermediate tail shocks and redirects the flow towards one side of the launcher. Finally, the wedge deflector generates a detached shock wave with a higher pressure increase than the inclined deflector. However, as the flow is redirected towards the two sides, a lower OASPL reaches the fairing. In the same way, the pressure distribution over the fairing surface has shown that the wedge deflector is acoustically more efficient for this case of study. The acoustic effectiveness of deflectors has been demonstrated compared to the case without a deflector. Therefore, deflectors are advised to be included on the launch platform to improve payload comfort and reliability on the launchers.

1. Introduction

The launch industry has grown more competitive due to the expansion of commercial space companies to broaden access to space [1]. To attract customers seeking reliable launchers, companies must differentiate themselves in payload requisites [2]. One of the most detrimental requirements in spacecraft design and manufacturing is the vibroacoustic load specification generated during lift-off [3,4], while unstable aerodynamic phenomena cause loads during flight [5]. The fairing, which houses the payload, protects it from thermal, acoustic, and mechanical loads. However, pressure fluctuations generate an intense diffuse acoustic field inside the fairing cavity [6,7]. Vibro-acoustic loads can damage payload components, especially antennas, and solar arrays, leading to mission failure [8]. In fact, up to 60% of the first-day satellite failures are attributed to excessive noise levels [9]. Therefore, mitigating acoustic loads reaching the fairing is essential for launch vehicle safety and successful operation.

Noise levels during lift-off are more significant than during flight [6,7]. At this stage, noise sources include turbulence at the mixing layer of the jet, shock-wave or Mach-associated noise, and impingement tones at the launch pad surface [10,11]. Moreover, the solid rocket engine generates dynamic excitation from pressure oscillations, typically damped by structural elements [12].

Various techniques for reducing noise are in use, including internal methods like acoustic blankets [13,14] and external methods at the launch pad level, such as water injection [15], sonic crystals [16], and perforated plates [17]. Launch pads typically feature a service tower, exhaust ducts, and a deflector. The exhaust duct and deflector redirect the hot and high-speed rocket plume, impacting the deflector, producing dominant acoustic waves [3].

The power of these acoustic waves is related to the strength of the plate shock wave [18]. As the rocket lifts off, the exhaust impacts the launch platform, becoming the main noise source [19]. Thus, properly designing the exhaust ducts and deflector helps mitigate the acoustic waves propagating towards the fairing. Different deflector arrangements exist, such as closed deflectors with closed ducts and single-sided and multiple-sided deflectors [3]. Acoustic efficiency, measured as the ratio of sound power to rocket exhaust mechanical power, varies among deflector types [20]. The mechanical power of the jet exhaust is the product of the engine thrust and the jet exit velocity. While sound power is the rate at which sound energy is generated and radiated. The acoustic efficiency of undeflected jets is 0.22%, while flat deflectors at six diameters exhibit the lowest efficiency. Bucket deflectors with a

* Corresponding author at: R&D Department, Comet Ingeniería, Convento Carmelitas, 2, Valencia, 46010, C.V., Spain.
E-mail address: mescarti@comet-ingenieria.es (M.S. Escartí-Guillem).

https://doi.org/10.1016/j.actaastro.2023.09.005
Received 26 February 2023; Received in revised form 19 July 2023; Accepted 7 September 2023
Available online 20 September 2023

duct have an efficiency closest to undeflected jets, around 0.16%. Cone-shaped deflectors have a low efficiency of roughly 0.05%, while a 45° inclined plate has a medium efficiency of 0.10% [21].

Different launch pads employ various deflector shapes. For example, the Space Shuttle launch pad, as well as the VEGA launch pad, include a wedge deflector [22], and JAXA developed an inclined deflector for the Epsilon launcher [18]. However, the underlying mechanisms of acoustic waves during lift-off are not yet fully understood. Thus, understanding the aeroacoustic characteristics of different flame deflectors is crucial, as a properly designed deflector can reduce sound levels.

Understanding the phenomena causing acoustic loads is crucial for minimizing them. Experimental measurements near the jet during launch are impossible due to the hostile environment [20]. Therefore, several prediction techniques have been developed, which include empirical investigations, sub-scale model experiments, and numerical models [6,20]. Though widely used, the empirical NASA SP-8072 model mainly predicts Mach wave radiation from the free jet [18,23]. Researchers have modified it to improve accuracy [24,25], but they often neglect critical aspects like sound motion and launch pad structures. Despite the adjustments, the empirical models still poorly agree with experimental results [26], which is why they are inappropriate for noise control design.

On the other hand, scaled model experiments are used to examine the phenomenon [27–30], but maintaining consistency with the actual launch event is challenging [3]. Relevant information on the interaction of the impingement flow can be found in measurements, but providing detailed data near the jet is impossible due to high temperatures and velocities [3,26].

Numerical analyses have the advantage of providing precise information on the flow behavior [31,32]. Computational Fluid Dynamics, CFD, thanks to algorithms and supercomputer capability advancements, allows more affordable studies than the equivalent experiment. Large Eddy Simulations, LES, has shown good accuracy in predicting supersonic free jet aeroacoustic [33] and shock waves [34]. However, the numerical model should be able to analyze the turbulent boundary layer on the walls. This is still unfeasible in LES due to the computational expense of a wall-resolved algorithm and computing all the launch platform domains [23,26]. To address this, some studies use CFD for noise generation and Computational Aeroacoustics, CAA, for sound propagation [23,35,36].

This work employs the same CFD model to resolve the noise generation and propagation as in [31]. In [37], we proposed a turbulence modeling simplification to decrease the computational cost with an Unsteady Reynolds-averaged Navier–Stokes (URANS) model. Both in [37,38], the model prediction showed good accuracy with experimental data. With this numerical model, we aim to analyze the effect of the deflector shape on the acoustic environment during lift-off. The goal is to assess the noise sources and their propagation to the fairing. In addition to the near field, the pressure field on the fairing is studied as a novelty in this work. As the acoustic loads on the fairing impose severe restrictions on the payload, it is crucial to understand how the different deflectors affect the acoustic field reaching the fairing. The study focuses on the Vega launcher [7,39], considering three deflector shapes: the actual wedge deflector, a 30° inclined deflector, and a flat deflector as the worst-case scenario from an acoustic perspective.

The structure of this work includes methods for the numerical prediction modeling described in Section 2, findings and results in Section 3, and conclusions of the work are summarized in Section 4.

2. Methods

2.1. Numerical model

The free software OpenFOAM v1912 [40] is used to perform the simulations. The approach to model turbulence is based on Unsteady Reynolds-Averaged Navier–Stokes [41].

Table 1
Boundary and initial conditions.

	Internal field	Inlet	Outlet	Walls
U (m/s)	Uniform 0	FixedValue 2713	ZeroGRadient	NoSlip
P (Pa)	Uniform 101 325	TotalPressure p_0 9.5e6	WaveTransmissive	ZeroGradient
k (m^2/s^2)	Uniform 9746	Uniform 9746	ZeroGradient	kqRWallFunction 1e−15
T (K)	Uniform 293	FixedValue 1699	ZeroGradient	ZeroGradient
ω (1/s)	Uniform 1.37e6	FixedValue 1.37e6	ZeroGradient	OmegaWallFunction 5.73046e7

The URANS equations are the usual RANS equations. We refer to it as Unsteady-RANS by convention because we retain the transient term in the computation. A limitation of the URANS model is that instead of resolving the turbulence scales, it models them through an effective eddy viscosity introduced by the Boussinesq approximation. Moreover, due to the transient nature of the model, information on pressure variations caused by shock waves and the average of turbulence can be collected. The turbulence model chosen is the two-equation eddy-viscosity model $k-\omega$ SST [42]. This model combines $k-\omega$ in the near-wall zones with $k-\epsilon$ in the free-flow region.

The rhoPimpleCentralFoam solver [43] is used, employing a compressible pressure-based coupled solver with Kurganov and Tadmor central-upwind schemes. Discretization schemes include first-order upwind for convective terms, first/second-order limited linear for the rest of the variables, and second-order linear for Laplacian terms. The second order van Leer interpolation scheme [44] is used for better shock wave definition [45]. An implicit first-order Euler scheme is used for time discretization. Stability is ensured by setting the Courant–Friedrichs–Lewy number (CFL) to CFL<0.3, as recommended for supersonic flows [43]. The initial time step is set to $1e^{-7}$, although later is defined by the CFL, and the total simulated time is 200 ms due to computational constraints [43]. Inlet conditions are applied at the end of the rocket nozzle, calculated using isentropic flow equations and reference information [46,47]. The boundary conditions are those shown in Table 1.

Three deflector geometries are analyzed, including a flat deflector, 30° inclined deflector, and wedge-type deflector, as shown in Fig. 1. The geometry of the Vega launch vehicle, whose length is 30 m, has also been included in the model. The exhaust ducts have a length of 90 m, therefore, the fluid domain considered has a size of 200 × 200 × 200 m.

Two structured hexahedral meshes have been generated for each case with different refinements. For this purpose, the computational volume is discretized using the SnappyHexMesh tool. The study of mesh independence in such a large domain is unfeasible due to its high computational cost. Therefore, a mesh independence study has been performed only for the area near the rocket engine plume. The results of the study can be found in [48]. High mesh resolution has been imposed in the plume region to resolve the acoustic source regions along the launch vehicle in both meshes. For efficiency, the rest of the mesh gets coarser as it gets closer to the far field domain boundaries, as seen in Fig. 1(c). The mesh slice depicted in Fig. 1(c) only shows the mesh close to the launch vehicle. The first set of meshes presents fewer elements due to a lack of computational power. To achieve an improved spatial resolution of the propagating waves, the second set of meshes has been meshed more uniformly and with higher resolution around the vehicle following the results concluded in [48]. In addition, a uniform element size has been maintained in the boundary layer to satisfy the requirements of the wall functions. The total number of elements is shown in Table 2 together with the element size in the plume region.

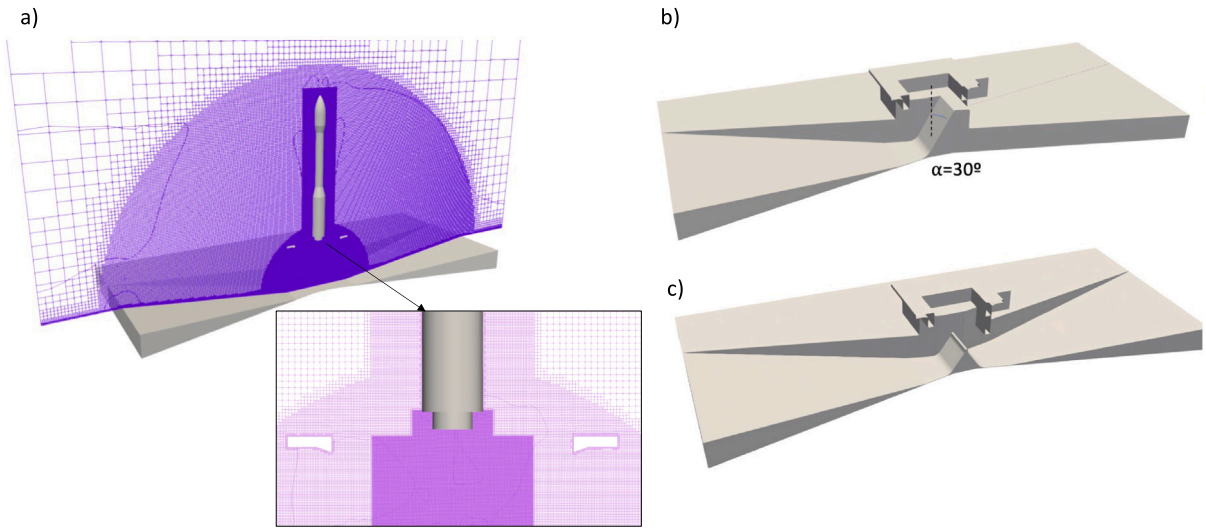

Fig. 1. Launch platform geometry. (a) Flat plate deflector. (b) Inclined deflector. (c) Wedge deflector.

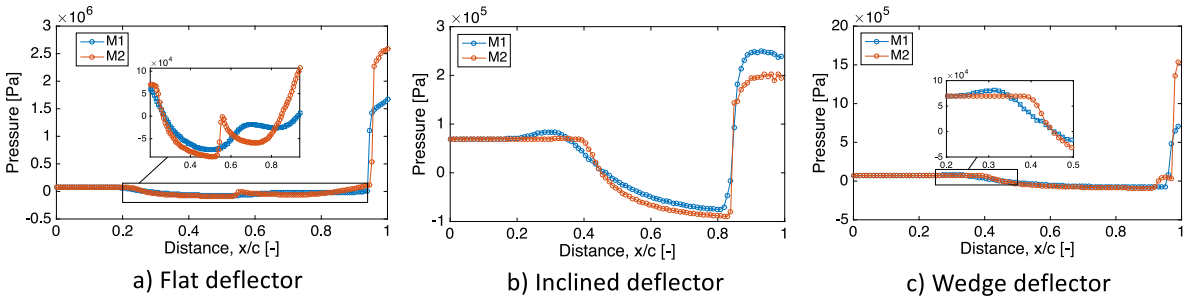

Fig. 2. Influence of the mesh on the center line pressure Deflector: (a) flat, (b) inclined, and (c) wedged.

About 9 points per wavelength are maintained in the acoustic region. Based on the speed of sound, the maximum frequency resolved is 2 kHz for the refined meshes.

2.2. Computational cost

From previous work and the information available in the literature [31,37,45], it is clear that it is necessary to perform the calculations with a large spatial discretization. This results in a high computational cost. The three simulations from the first set of meshes have been calculated in the cluster Rigel from Universitat Politècnica de València. For this simulation, 128 processors were used per case. The second set of meshes that require a higher computational effort has been calculated in the MareNostrum supercomputer from the Barcelona Supercomputing Center. The computations were performed with 2160 processors per simulation. The computations took around three months, totaling 5 882 000 h, to simulate 200 ms for each configuration.

3. Results and discussion

3.1. Sensitivity analysis of mesh resolution

First, the effect of the two meshes is assessed for each configuration. The pressure distribution on the jet centerline starting at the nozzle is shown in Fig. 2. The distance has been normalized between 0 (exit of the nozzle) and 1 (deflector surface) since the length between the nozzle and the ground varies for each configuration.

In all three configurations, the pressure is consistent for both meshes up to a distance of 0.2, corresponding to the jet core. Beyond that point, M2 shows a decrease in pressure due to a shock wave, while

Table 2
Details about the coarse and fine meshes in each case.

	Coarse Mesh - M1		Fine Mesh - M2	
	Cell size in jet region	Number of elements	Cell size in jet region	Number of elements
Flat		10,411,702		124,746,731
Inclined	0.039 m	10,382,724	0.019 m	107,460,587
Wedge		16,945,228		141,038,619

M1 exhibits a slight increase, as seen in cases (b) and (c). The less refined mesh predicts a slightly higher pressure along the section where pressure decreases. The flat deflector configuration, having a longer development length of the rocket plume, generates more shock waves, as shown in Fig. 3 . However, M1 fails to accurately predict the set of shock waves generated for this case, as depicted in Fig. 2(a). In comparison, M2 predicts a pressure jump around $x/c = 0.55$, consistent with a Mach diamond.

For the inclined deflector, both predictions exhibit a similar trend, highlighting the position of the stop zone on the wall. The main difference is that M1 predicts a higher pressure, likely due to insufficient points for a more accurate calculation. In the case of the wedge deflector, M1 predicts a sudden pressure jump near the wall due to the detached shock wave on the deflector. In contrast, M2 predicts a preliminary increase before the pressure jump, possibly due to the effect of the shock wave. In addition, the predicted pressure maximum is higher for M2.

These results indicate that while M1 captures the general flow behavior, it fails to make accurate predictions. Additionally, the more refined mesh is capable of capturing more sound waves. The smaller

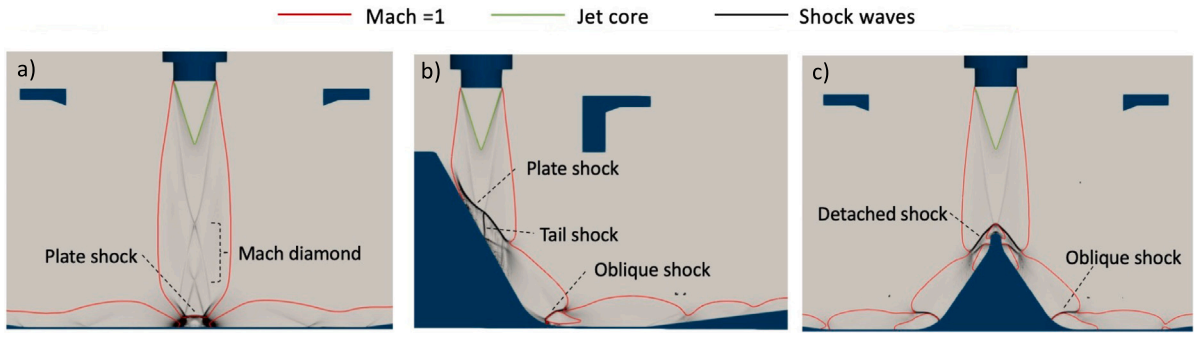

Fig. 3. Numerical Schlieren figures. The green line represents the jet core, the red line is the isoline where the Mach number is one, and the black lines represent shock waves. Deflector: (a) flat, (b) inclined, and (c) wedged. (For interpretation of the references to color in this figure legend, the reader is referred to the web version of this article.)

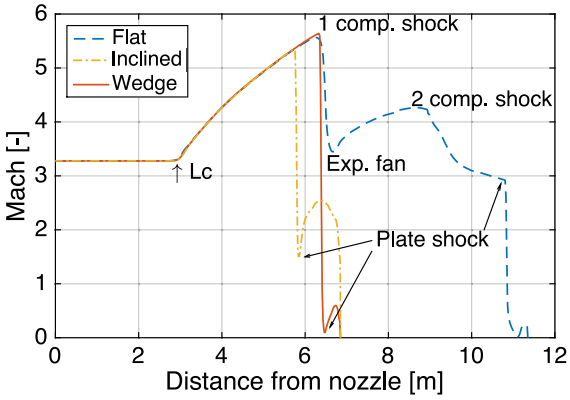

Fig. 4. Mach distribution along the jet axis.

mesh, with larger cell sizes, filters out or dissipates these waves, neglecting their influence. Notably, the computational cost of M2 is 11.25 times higher than that of M1. Since there are discrepancies between the results obtained with both meshes, if an accurate study is intended, the results of M2 should be assessed. However, simulations with M1 can provide a general understanding of flow behavior and the generated shock waves.

3.2. Noise sources identification: shock waves

The exhaust jet produces turbulence in the turbulent mixing layer, shock wave-associated noise, and surface reflections during launch. Identifying the shock waves each deflector creates is crucial for determining the areas where noise is generated. It should be noted that the jet velocity and the relative position between the jet and walls influence the distribution of the shock waves. The initial jet conditions are identical for all cases, so the set of waves generated results from the deflector arrangement. Fig. 3 presents the prediction of shock waves from numerical Schlieren images, indicating regions of turbulence generation with red isolines representing a Mach number of one, and the jet core displayed in green. The length of the jet core, Lc, remains constant across all configurations, as observed quantitatively in Fig. 4, where the Mach number distribution along the axis is shown.

For the flat deflector, more shock waves appear due to the greater length of jet development, resulting in a higher amount of associated acoustic energy. A Mach diamond formed by a set of compression shock waves is also observed. Fig. 4 illustrates the first compression wave is caused by higher ambient pressure. Given the rapid pressure increase, a train of expansion waves appears, resulting in a second shock wave that compresses the flow and reduces the Mach number. In addition, as expected, a plate shock wave emerges just above the stagnation bubble on the wall. The Mach one isoline reveals a larger area belonging to the jet, indicating a more significant amount of acoustic energy resulting from the turbulent mixing layer.

Fig. 3(b) shows the inclined deflector generating a plate shock over the deflector surface. An intermediate tail shock emerges where the jet shock connects with the plate shock, which then reflects between the wall and the slip line. These results align with experimental observations by Nakai et al. [49]. Furthermore, the change in flow direction due to the deflector curvature at the end of the ramp generates an oblique shock wave. The shock waves on the Mach isolines indicate the separation between the three central regions: the free jet, the impingement, and the wall jet. These shock waves generate a sequence of pressure peaks, with the strongest observed at the plate shock. Due to the shock wave reflections and a stagnation bubble, the plate shock is generated closer to the nozzle than the wedge defelctor, as shown in Fig. 4.

Finally, for the wedge-shaped deflector, Fig. 3(c) displays a detached shock wave on the deflector resulting from the advance of the jet's normal shock wave deforming on the deflector. The two curvature changes also generate oblique shock waves. As the jet develops on both sides of the deflector, the enclosed area by the Mach one isolines is larger compared to the inclined deflector. Compared to the inclined deflector, the plate shock appears at a greater distance from the nozzle and with a higher Mach number, resulting in a more intense shock wave.

3.3. Acoustic waves propagation

The pressure field around the payload is influenced by noise sources and wave propagation up to the fairing, encouraging space agencies to study different deflector designs to modify the sound field reflection. Hence, we analyze the pressure gradient field for each deflector at t = 0.05 s and t = 0.1 s in Fig. 5.

At the initial instant, spherical propagation of different waves centered at the exhaust jet is observed in all cases. The most significant gradients occur at the shock waves, as expected. Additionally, a set of lower-intensity waves resulting from engine ignition can be distinguished, ranging from blue to yellow, reaching the middle of the launch vehicle. The second set of waves, colored in red, corresponds to the reflection of the exhaust gases with the duct surfaces. The pressure gradient due to the exhaust jet reflection is more pronounced in all three cases, emphasizing the importance of controlling these phenomena. The inclined deflector redirects the flow to one side (Fig. 5a), the flat plate reflects the exhaust gases in all directions (Fig. 5b), and the wedge deflector redirects the flow towards both sides of the exhaust channels (Fig. 5c).

After 0.1 s, in the inclined deflector configuration, Fig. 5(d), the intense front wave resulting from the initial jet impingement has propagated in the ramp and up to the middle of the fairing. Despite the deflector redirecting the main flow, pressure waves due to the free jet region propagate before reaching the deflector. The propagation of the

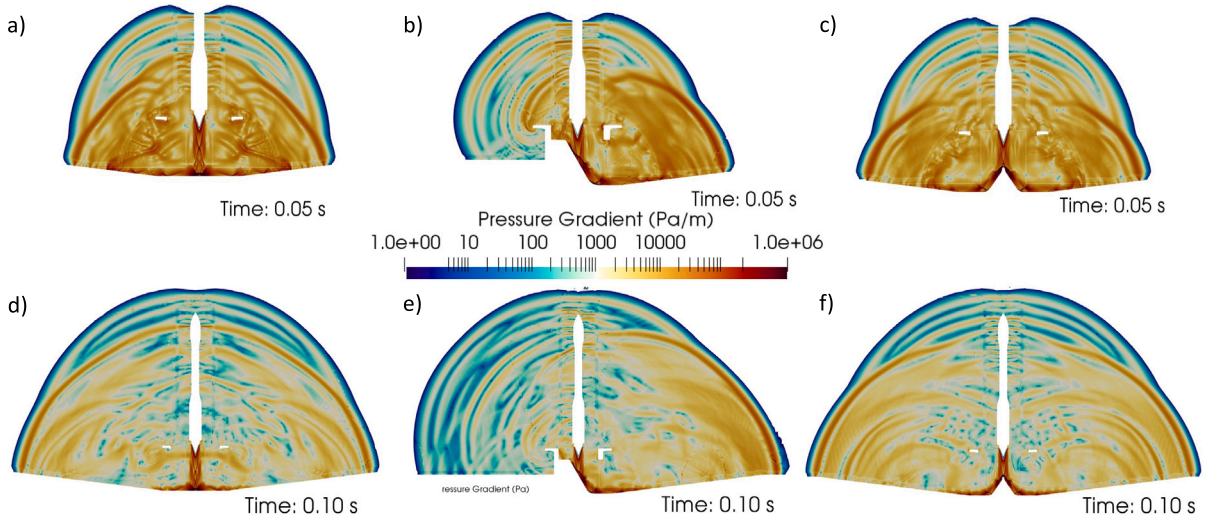

Fig. 5. Pressure gradient in logarithmic scale for the three configurations at t = 0.05 s (a, b and c) and at t = 0.1 s (d, e, f). (For interpretation of the references to color in this figure legend, the reader is referred to the web version of this article.)

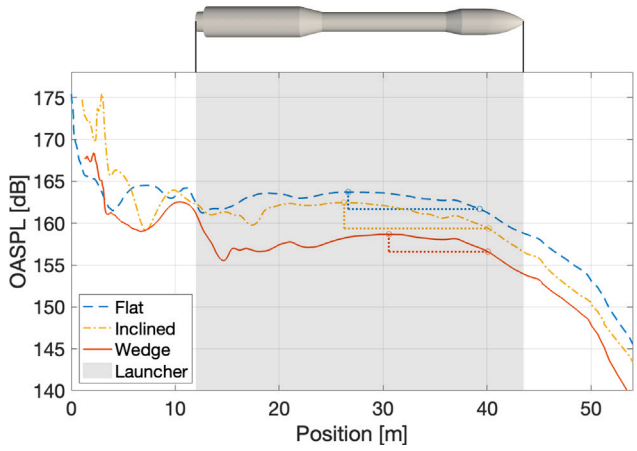

Fig. 6. Overall sound pressure level evolution along a vertical line along the rocket.

pressure gradient field in the flat case, Fig. 5(e), causes the wavefront to reach the fairing, exhibiting non-homogeneous pressure gradients due to the shape of the exhaust channels and floor slope. In the case of the wedge-shaped deflector, the flow is effectively separated in both directions of the exhaust ducts. Thus, the larger pressure gradient is pushed away from the fairing.

To analyze the effect of different waves on the acoustic field around the launcher, Sound Pressure Levels, SPL, are calculated using the Fast Fourier Transform. Measurement points are placed along a vertical line in the fluid domain at 2 m from the vehicle center. Each point has collected 376 samples spreading over 0.19 s with a time step of $5e^{-4}$ seconds. A Hanning windowing with 50% of overlapping is applied, resulting in the narrow band spectra resolution of 5 Hz, with a maximum valid frequency of 1000 Hz.

Fig. 6 shows the Overall Sound Pressure Level, OASPL, along the vertical line, comparing the results for the three configurations. Higher OASPLs are observed in the source region, with the inclined deflector generating a higher OASPL between 0 and 6 m. The inclined deflector redirects the flow to one side, while the other deflectors redirect the flow to both sides, resulting in higher levels.

At 7.5 m, the inclined and wedge deflectors present a drop, whereas the flat deflector exhibits a peak due to a shock wave not generated in the other cases, as seen in Fig. 4. Therefore, it is clear that the two deflectors reduce the acoustic load on the source by reducing the jet development length. At 10 m, OAPLS increases due to reflections caused by the rocket support. The gray area represents the location of the launch vehicle. In the first meters around the launcher, the OASPL measured at the wedge deflector case is reduced by approximately 7 dB. After 20 m, the OASPL variates slowly for all the cases.

In Fig. 6, a circle highlights the maximum level close to the fairing, and the next circle represents a 3 dB reduction. The flat configuration has the highest maximum value, followed by the inclined deflector, while the wedge deflector shows a 5 dB decrease. The horizontal line connecting both points represents the distance to achieve a 3 dB reduction. The inclined and flat configurations have similar length, while the wedge deflector, with lower OASPL values, achieves the 3 dB reduction faster. This is due to the wedge deflector redirecting the acoustic waves away from the center of the launch pad. Above the launcher, the OASPL decays more rapidly, indicating that the wedge deflector generates lower OASPL values near the vehicle.

3.4. Fairing pressure distribution

Having studied the noise propagation, the acoustic field around the fairing where the payload is located is analyzed. Fig. 7 shows the pressure distribution at the surface for the three deflector at three different time instants. At 0.08 s, the same pressure wave at the fairing tip, due to the rocket ignition blast wave, is present for all the configurations. The wedge configuration always presents smaller pressure values, which agrees with Fig. 6. The flat and wedge deflectors display symmetric pressure distributions, while the inclined deflector shows an asymmetrical distribution due to redirecting the flow to one side of the launch pad. This trend is repeated at all time steps.

Fig. 7(d) compares lines cutting the fairing in a sagittal plane to analyze asymmetry. The front line corresponds to the side where the inclined deflector redirects the flow, while the back side is shown with markers. The front and back lines coincide for flat and wedge deflectors, indicating symmetry of the acoustic field around the fairing. The platforms with flat and wedge deflectors are symmetrical from left to right but not radially. In contrast, the inclined deflector platform lacks symmetry due to the shape of the exhaust ducts, as shown in Fig. 7. This asymmetry of loads at the fairing surface can negatively impact structural response, a disadvantage of inclined deflectors.

Finally, Fig. 8 presents the time pressure signal for two different fairing heights. At h = 35.8 m (Fig. 8a), the gases reach the point at 0.066 s, while at h = 40 m (Fig. 8c), they reach it at 0.88 s due

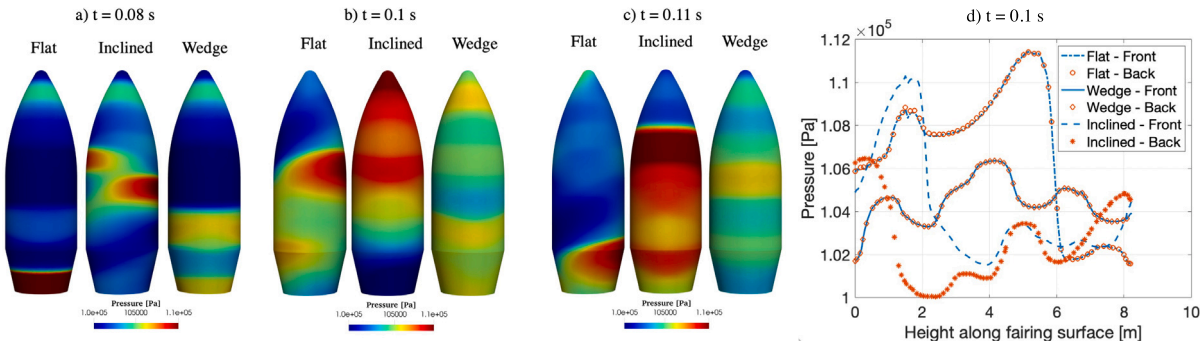

Fig. 7. Pressure contour at the fairing surface at t = 0.08 s (a), t = 0.1 s (b) and t = 0.11 s (c) and pressure distribution at t = 0.1 s (d).

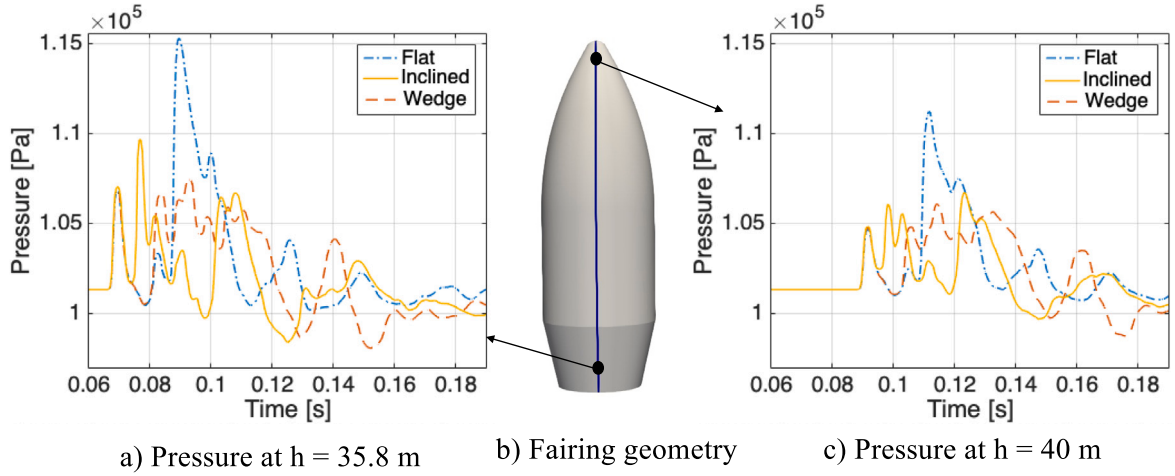

Fig. 8. Pressure time signal at different points of the fairing surface.

to the height difference. The wave pressure magnitude decreases with distance. The first peak represents the blast wave caused by ignition over-pressure and is independent of deflector geometry. After this initial wave, each geometry generates different acoustic waves. The flat geometry produces the highest peak pressure, while the wedge deflector generates the smallest. Therefore, the use and shape of the deflector modify the acoustic field propagating during lift-off.

4. Conclusions

With the increasing competitiveness of the launch vehicle business, reducing the dynamic loads generated is crucial. In addition, it is necessary to design additional launch platforms for emerging launch vehicles. Experimental measurements during lift-off are challenging due to harsh conditions. Hence, this study analyzed the impact of plume deflectors on the acoustic environment during lift-off using computational fluid dynamics techniques. Three deflector geometries were studied for the Vega launch vehicle: wedge, inclined, and flat deflectors. The inclined deflector generated plate and tail shocks, while the wedge deflector had a detached shock and higher pressure raise. The flat deflector produced a Mach diamond and more shock waves, producing higher acoustic energy. Since there is no reflection during the first engine outflow, blast wave propagation is similar for all designs. Pressure wave propagation and reflections were observed, influenced by shock waves and pressure gradient. Higher pressure gradients are primarily created by shock waves and exhaust gas reflection on surfaces, highlighting the need to minimize these effects. The inclined deflector redirected the flow to one side, the wedge deflector redirected to both sides, and the flat deflector reflected pressure waves equally in all directions, leading to higher-intensity waves reaching the fairing. In contrast, the wedge deflector generated the lowest OASPL along the longitude of the launcher. Pressure distribution at the fairing showed symmetrical azimuthal patterns for the wedge and flat deflectors, while the inclined deflector was asymmetrical. On the fairing surface, the flat deflector produces the highest pressure peaks, followed by the inclined deflector, and the wedge deflector produces the lowest peaks. Additionally, it has been found that the wedge-type deflector can reduce the acoustic stresses that reach the fairing.

Through this work, the phenomena of noise generation and propagation for different rocket plume deflectors have been observed. The CFD technique has enabled this analysis since it provides information that is currently impossible to collect experimentally. The findings of the study highlight the importance of controlling noise effects and demonstrate the acoustic effectiveness of deflectors in reducing acoustic loads during launch vehicle lift-off.

Declaration of competing interest

The authors declare that they have no known competing financial interests or personal relationships that could have appeared to influence the work reported in this paper.

Acknowledgments

Authors acknowledge the support of the European Space Agency, France under contract 4000126316/19/NL/LvH of project REDLAUCH: Launch Sound Level Reduction. This work has the support of grant PID2021-128676OB-I00 funded by MCIN/AEI/10.13039/501100011033 and by “ERDF A way of making Europe”, by the “European Union”. The work was supported by the Spanish Ministry of Science and Innovation through project PID2019-109175GB-C22 Mineco/FEDER. Part of the simulations have been performed on

MareNostrum (BSC) with the project IM-2021-2-0017 Rocket launch aeroacoustic. L.M. García-Raffi is grateful for the partial support by the Grant PID2020-112759GB- I00 funded by MCIN/AEI/10.13039/501100011033.

References

[1] G. Denis, D. Alary, X. Pasco, N. Pisot, D. Texier, S. Toulza, From new space to big space: How commercial space dream is becoming a reality, Acta Astronaut. 166 (2020).
[2] B. Chemoul, E. Louaas, P. Roux, D. Schmitt, M. Pourcher, Ariane 5 flight environments, Acta Astronaut. 48 (5) (2001).
[3] C. Jiang, T. Han, Z. Gao, C.H. Lee, A review of impinging jets during rocket launching, Prog. Aerosp. Sci. 109 (2019).
[4] D. Sziroczak, H. Smith, A review of design issues specific to hypersonic flight vehicles, Prog. Aerosp. Sci. 84 (2016).
[5] R. Camussi, A. Di Marco, C. Stoica, M. Bernardini, F. Stella, F. De Gregorio, F. Paglia, L. Romano, D. Barbagallo, Wind tunnel measurements of the surface pressure fluctuations on the new VEGA-c space launcher, Aerosp. Sci. Technol. 99 (2020).
[6] ECSS, Spacecraft mechanical loads analysis handbook, Eur. Coop. Space Stand. (2013).
[7] VEGA user's manual. Issue 4, 2014.
[8] J.P. Arenas, R.N. Margasahayam, Ingen. Revista Chil. Ingen. 14 (3) (2006).
[9] S. Griffin, S. Lane, D. Leo, Innovative vibroacoustic control approaches in space launch vehicles, 2000.
[10] C.K. Tam, Supersonic jet noise, Annu. Rev. Fluid Mech. 27 (1) (1995).
[11] T. Nonomura, H. Nakano, Y. Ozawa, D. Terakado, M. Yamamoto, K. Fujii, A. Oyama, Large eddy simulation of acoustic waves generated from a hot supersonic jet, Shock Waves 29 (8) (2019).
[12] A. Rittweger, S. Muller, J.-F. Durand, The new approach for damping modelling in the coupled dynamic load analysis for the ariane 5 acoustic booster mode load cases, Acta Astronaut. 81 (2) (2012).
[13] S. Frikha, M.A. Hamdi, P. Roux, L. Mebarek, Noise reduction prediction of ariane 5 fairing with acoustic protection made of porous-elastic material, J. Acoust. Soc. Am. (2008).
[14] A.C. Abeel, E.M. Wooldridge, M. Calcabrini, J.O. Ward, O. Schmeitzky, Overview of contamination control for the james webb space telescope launch campaign, in: Space Systems Contamination: Prediction, Control, and Performance 2022, vol. 12224, SPIE, 2022.
[15] A. Vorobyov, T. Abdurashidov, V. Bakulev, A. But, A. Kuznetsov, A. Makaveev, Problem of intensity reduction of acoustic fields generated by gas-dynamic jets of motors of the rocket-launch vehicles at launch, Acta Astronaut. 109 (2015).
[16] L. Garcia-Raffi, L. Salmerón-Contreras, I. Herrero-Durá, R. Picó, J. Redondo, V. Sánchez-Morcillo, K. Staliunas, N. Adkins, A. Cebrecos, N. Jiménez, V. Romero-García, Broadband reduction of the specular reflections by using sonic crystals: A proof of concept for noise mitigation in aerospace applications, Aerosp. Sci. Technol. 73 (2018).
[17] S. Vasilieva, I. Guk, S. Medvedev, S. Khomik, Experimental and numerical study of perforated plates effectiveness to ensure safety in case of emergencies on spacecraft and launch pads, Acta Astronaut. (2022).
[18] S. Tsutsumi, Design of launch pad for mitigating acoustic loads on launch vehicle at liftoff, J. Acoust. Soc. Korea 39 (2020).
[19] J. Panda, R.N. Mosher, B.J. Porter, Noise source identification during rocket engine test firings and a rocket launch, J. Spacecr. Rockets 51 (2014).
[20] K.M. Eldred, Acoustic loads generated by the propulsion system, Tech. rep., NASA Technical Reports Server, 1971.
[21] J. Cole, R. England, R. Powell, Effects of various exhaust blast deflectors on the acoustic noise characteristics of 1000 pound thrust rockets, 1960, WADDTR60-6.
[22] R. Picó, I. Herrero-Durá, V. Sánchez-Morcillo, L. Salmerón-Contreras, L. Garcia-Raffi, Acoustic behavior of the VEGA launch pad environment, Proc. EuroReg. (2016).
[23] C. Xing, G. Le, L. Shen, C. Zhao, H. Zheng, Numerical investigations on acoustic environment of multi-nozzle launch vehicle at lift-off, Aerosp. Sci. Technol. 106 (2020).
[24] J. Varnier, Experimental study and simulation of rocket engine freejet noise, AIAA J. 39 (10) (2001).
[25] K.J. Plotkin, L.C. Sutherland, B.T. Vu, Lift-off acoustics predictions for the ares I launch pad, 2009.
[26] C.P. Lubert, K.L. Gee, S. Tsutsumi, Supersonic jet noise from launch vehicles: 50 years since nasa SP-8072, J. Acoust. Soc. Am. 151 (2) (2022).
[27] J. Panda, R. Mosher, Microphone phased array to identify liftoff noise sources in model-scale tests, J. Spacecr. Rockets 50 (2013).
[28] P. Malbéqui, R. Davy, C. Bresson, Experimental characterization of the acoustics of the future ariane 6 launch pad, in: 7th European Conference for Aeroacoustics and Space Science (EUCASS), 2017.
[29] G. Dumnov, D. Mel'Nikov, V. Komarov, Acoustic loads on rockets during launch, in: 36th AIAA/ASME/SAE/ASEE Joint Propulsion Conference and Exhibit, 2000.
[30] N. Karthikeyan, L. Venkatakrishnan, Acoustic characterization of jet interaction with launch structures during lift-off, J. Spacecr. Rockets 54 (2017).
[31] M.S. Escarti-Guillem, S. Hoyas, L.M. García-Raffi, Rocket plume URANS simulation using openfoam, Res. Eng. 4 (2019).
[32] S. Hoyas, M. Oberlack, S. Kraheberger, F. Álcantara-Ávila, J. Laux, Wall turbulence at high friction Reynolds numbers, Phys. Rev. Fluids (2021).
[33] K. Fukuda, S. Tsutsumi, K. Fujii, K. Ui, T. Ishii, H. Oinuma, J. Kazawa, K. Minesugi, Acoustic measurement and prediction of solid rockets in static firing tests, in: 15th AIAA/CEAS Aeroacoustics Conference (30th AIAA Aeroacoustics Conference by the American Institute of Aeronautics and Astronautics, Inc., 2009.
[34] R. Kamali, S.M. Mousavi, A.R. Binesh, Three dimensional CFD investigation of shock train structure in a supersonic nozzle, Acta Astronaut. 116 (2015).
[35] P.A. Liever, J.S. West, R.E. Harris, Validation of high-fidelity CFD/CAA framework for launch vehicle acoustic environment simulation against scale model test data, in: JANNAF Conference, 2016, no. M17-5678.
[36] Hybrid discontinuous galerkin and finite volume method for launch environment acoustics prediction, 52, American Institute of Aeronautics and Astronautics Inc., 2015,
[37] M.S. Escartí-Guillem, L.M. García-Raffi, S. Hoyas, URANS analysis of a launch vehicle aero-acoustic environment, Appl. Sci. 12 (7) (2022).
[38] M.S. Escarti-Guillem, L.M. Garcia-Raffi, S. Hoyas, O. Gloth, Assessment of computational fluid dynamics acoustic prediction accuracy and deflector impact on launch aero-acoustic environment, in: Proceedings of Meetings on Acoustics, vol. 50, AIP Publishing, 2022, (1).
[39] S. Bianchi, VEGA, the European small launcher: Development status, future perspectives, and applications, Acta Astronaut. 63 (1) (2008) Touching Humanity - Space for Improving Quality of Life. Selected Proceedings of the 58th International Astronautical Federation Congress, Hyderabad, India, 24-28 September 2007.
[40] H.G. Weller, G. Tabor, H. Jasak, C. Fureby, A tensorial approach to computational continuum mechanics using object-oriented techniques, Comput. Phys. 12 (6) (1998).
[41] D.C. Wilcox, Formulation of the kw turbulence model revisited, AIAA J. 46 (11) (2008).
[42] F. Menter, Zonal two equation kw turbulence models for aerodynamic flows, in: 23rd Fluid Dynamics, Plasmadynamics, and Lasers Conference, 1993.
[43] M.V. Kraposhin, M. Banholzer, M. Pfitzner, I.K. Marchevsky, A hybrid pressure-based solver for nonideal single-phase fluid flows at all speeds, Internat. J. Numer. Methods Fluids 88 (2) (2018).
[44] B. Van Leer, Towards the ultimate conservative difference scheme. II. Monotonicity and conservation combined in a second-order scheme, J. Comput. Phys. 14 (4) (1974).
[45] M.S. Escarti-Guillem, L.M. Garcia-Raffi, S. Hoyas, O. Gloth, Assessment of computational fluid dynamics acoustic prediction accuracy and deflector impact on launch aero-acoustic environment, in: Proceedings of Meetings on Acoustics, 50, (1) AIP Publishing, 2022.
[46] L. Marigliani, Numerical analysis of solid rocket motor plume radiative heat transfer at low altitude, 2017.
[47] M. Calabro, E. Gizzi, N. Wingborg, Y. Batonneau, R. Beauchet, C. Kappenste, Propellant Requirements and Future Demands, Tech. rep., GRAIL Ref. Ares(2016)501389, 2016.
[48] F.N. Ramírez, M.S. Escarti-Guillem, L.M. García-Raffi, S. Hoyas, A study of the mesh effect on a rocket plume simulation, Res. Eng. 13 (2022).
[49] Y. Nakai, N. Fujimatsu, K. Fujii, Experimental study of underexpanded supersonic jet impingement on an inclined flat plate, AIAA J. 44 (11) (2006).